Enhanced Stark Tuning of Single InAs (211)*B* Quantum Dots due to Nonlinear Piezoelectric Effect in Zincblende Nanostructures

S. Germanis,[1,2] C. Katsidis,[1] S. Tsintzos,[2] A. Stavrinidis,[2] G. Konstantinidis,[2] N. Florini,[3] J. Kioseoglou,[3] G. P. Dimitrakopulos,[3] Th. Kehagias,[3] Z. Hatzopoulos,[2,4] and N. T. Pelekanos[1,2,*]

[1]*Department of Materials Science and Technology, University of Crete, P.O. Box 2208, 71003 Heraklion, Greece*
[2]*Microelectronics Research Group, IESL-FORTH, P.O. Box 1385, 71110 Heraklion, Greece*
[3]*Physics Department, Aristotle University of Thessaloniki, 54124 Thessaloniki, Greece*
[4]*Department of Physics, University of Crete, P.O. Box 2208, 71003 Heraklion, Greece*

(Received 4 November 2015; revised manuscript received 19 April 2016; published 13 July 2016)

We report enhanced Stark tuning of single exciton lines in self-assembled (211)*B* InAs quantum dots (QDs) as a consequence of pronounced piezoelectric effects in polar orientations, making this QD system particularly sensitive to relatively "small" applied external fields. The Stark shifts in the first hundreds of kilovolts per centimeter of applied external field are at least 2.5 times larger, compared to those observed in nonpiezoelectric (100) InAs QDs of similar size. To account quantitatively for the observed transition energies and Stark shifts, we utilize a graded In-composition potential profile, as deduced from local strain analysis performed on high-resolution transmission microscopy images of the QDs. Our results provide a direct demonstration of the importance of nonlinear piezoelectric effects in zincblende semiconductors.

DOI: 10.1103/PhysRevApplied.6.014004

I. INTRODUCTION

Semiconductor quantum dots (QDs) are the ultimate sources of "on-demand" single photons [1], entangled-photon pairs [2], and indistinguishable photons [3], with direct applications in quantum cryptography and quantum-information processing schemes. In this direction, piezoelectric (PZ) QDs, i.e., QDs carrying in their central part a strong PZ field along the growth axis, offer concrete advantages compared to non-PZ QDs on several practical aspects of single- or entangled-photon sources. First, the large exciton-biexciton energy differences encountered in PZ QDs due to the strong PZ field, enable the two lines to remain resolved with increasing temperature, allowing for single-photon emission at high temperatures [4]. Second, the PZ field along the QD growth axis preserves the high symmetry of the confining potential [5], leading to negligible fine-structure splittings of the ground exciton state in as-grown QDs [5–7], which is a prerequisite for the generation of high-fidelity entangled photons [8]. Another interesting feature of PZ QDs explored in this work, is their high sensitivity to relatively "small" external electric fields due to the quadratic nature of the quantum-confined Stark effect (QCSE), giving rise to enhanced Stark tunings of their exciton lines and the possibility for widely tunable single-photon sources. Such sources open new possibilities in quantum-information experiments, including, for instance, enhancing the efficiency of a QD emitter by tuning it in resonance with a cavity mode [9], entangling the emission of two remote independent single QDs at the same energy [10], and fine-tuning the intermediate exciton state to suppress the fine-structure splitting [11].

In this paper, we focus on self-assembled InAs QDs grown on (211)*B* GaAs substrates [12]. The main motivation for using (211)*B* QDs is that they can be grown in the Stranski-Krastanow growth mode, which is not possible in the (111) orientation [13]. A key characteristic of these high-index-grown polar nanostructures is their possibility to exhibit pronounced strain-induced PZ fields, which can dramatically modify their electronic and optical properties. According to linear elasticity theory applied to cubic polar heterostructures [14], the PZ polarization P_{PZ} in a biaxially strained layer is proportional to the linear PZ coefficient e_{14} and the in-plane strain $\varepsilon_{//} = (a_s - a)/a_s$, where a_s and a are the lattice parameters of the substrate and epilayer, respectively. This description is often termed as the linear PZ effect, since higher-order terms of the strain tensor are neglected in the PZ polarization. It is well known [15,16] that e_{14} consists of two opposite-sign contributions: a purely "electronic" contribution versus an internal strain-induced one, often called simply "ionic." In III–V compound semiconductors, the electronic contribution exceeds the ionic one and e_{14} becomes negative, implying that if the crystal is expanded in the [111] direction, positive charges will appear on the *B* face. As an example, the experimental e_{14} values for GaAs and InAs are -0.16 and -0.045 $\mathrm{C/m^2}$, respectively [17]. In these experiments on bulk crystals, the strain values applied to the samples are minute, of the order of 10^{-6}, posing no real challenge to the linear PZ effect.

The situation changes considerably in the case of two-dimensional strained heterostructures, such as, for instance, InGaAs/GaAs quantum wells (QWs), where the typical

*Corresponding author.
pelekano@materials.uoc.gr

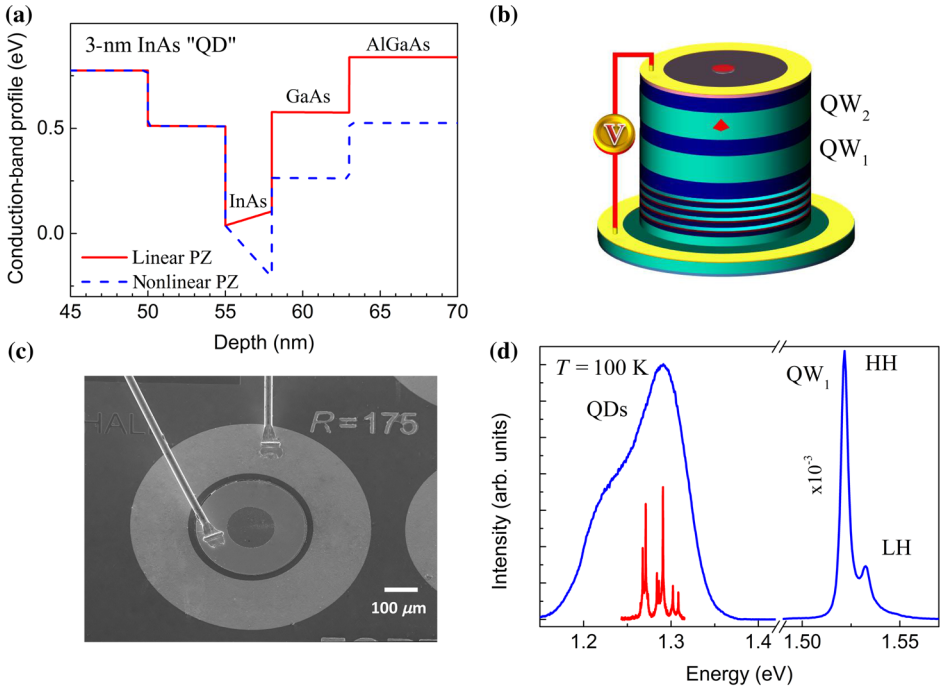

FIG. 1. (a) Conduction-band profiles of a 3-nm $(211)B$ InAs/GaAs QD illustrating the influence of the nonlinear PZ effect in reversing the direction of the internal field. (b) Schematic representation of the total diode structure. (c) Top view SEM image of a bonded device. (d) Macro-PL spectrum (blue line) from the active region of the diode, showing characteristic emission from the QDs and QW_1 at 100 K. The sharp-peaked spectrum in red is micro-PL emission through nanoapertures opened on the top metal layer.

lattice mismatch strain is about 1%. In such relatively high strains, it is likely that higher-order terms, nonlinear to strain, contribute to the PZ polarization. This is especially true in the case of InAs, where the near cancellation of the electronic and ionic contributions in e_{14} favors the observation of nonlinear PZ effects [18]. Indeed, an unexpected dependence of e_{14} on strain, as well as a significant deviation from the extrapolated values based on the binary e_{14} values has been demonstrated in strained $In_xGa_{1-x}As$ $(111)B$ QWs [19]. Evidence for nonlinear piezoelectricity has also been reported earlier in CdTe QWs [20,21].

In the case of high-index InAs/GaAs nanostructures, the situation is even more favorable for observing nonlinear PZ effects, considering the very high lattice strains that these nanostructures can sustain, reaching values up to 7%. Evidence for the existence of large PZ fields in $(h11)$ InAs QDs has been reported previously [22,23]. By using linear bulk InAs PZ coefficient, a PZ field of 250 kV/cm was estimated for (211) InAs QDs [22]. As a comparison, we note that this value is only a small fraction of the 7 MV/cm internal field observed in hexagonal c-axis-oriented GaN QDs [24,25]. However, late *ab initio* theoretical calculations of PZ coefficients in highly strained InAs have suggested that the quadratic terms in the PZ polarization are so important that they can reverse the direction of the PZ field in $(h11)$ InAs QDs and strongly enhance its amplitude, leading to values as high as 0.8 MV/cm in pure (211) InAs QDs [26]. Such strong fields are expected to fully dominate the optical and dynamic properties of $(h11)$ InAs QDs.

In this paper, having in mind the demonstration of a tunable single-photon emitter at elevated temperatures, we report an experimental study of QCSE on the emission of single $(211)B$ InAs/GaAs PZ QDs at 100 K. It should be noted that these QDs continue to behave as single-photon emitters at 100 K as directly confirmed by antibunching experiments. Accordingly, bias-dependent microphotoluminescence (μ-PL) experiments are performed on specially designed Schottky-diode samples containing the PZ QDs, revealing pronounced Stark *redshifts* of the QD emission lines under reverse bias. The direction of these shifts intelligibly demonstrates that the PZ field is opposite of that predicted based on the linear PZ coefficient, confirming the importance of nonlinear PZ effects in heavily strained zincblende nanostructures. This situation is schematically illustrated in Fig. 1(a), where the application of a reverse bias to the band profile with linear PZ effect will certainly lead to a *blueshift*, as opposed to a *redshift* in the case of the band profile with nonlinear PZ effects taken into account. The observed dot transition energies and Stark shifts are accounted for quantitatively, using a 1D effective mass approximation model and a graded In-composition profile deduced by geometric phase analysis (GPA) on high-resolution transmission-electron-microscopy (HRTEM) images of the QDs [27].

II. EXPERIMENT

The sample is grown by molecular beam epitaxy on a $(211)B$ GaAs semi-insulating substrate. The structure starts with a 1-μm-thick n^+GaAs buffer layer doped by 10^{18} cm^{-3} to be used as the bottom n contact. The intrinsic region contains first a 40-period 2.5 nm/1.6 nm GaAs/AlAs short-period superlattice serving as a high-quality template for the nucleation of QDs. Then follows the active region, which consists of three 50-nm-thick $Al_{0.3}Ga_{0.7}As$ barrier layers confining a first 12-nm-thick GaAs *reference* QW_1 for the

calibration of the actual electric field applied by the external bias and a second 10-nm-thick GaAs QW_2 containing the QD layer in the middle. The QD layer is formed in the Stranski-Krastanow mode by deposition of 1.5 ML of InAs at 500 °C with a growth rate of 0.1 ML/s. The sample ends with a 5-nm GaAs cap layer to protect the top $Al_{0.3}Ga_{0.7}As$ layer from oxidation. A twin sample with an uncapped QD layer grown on the top surface under the same conditions provides information about the QD structural characteristics by atomic force microscopy (AFM). The QDs have a density of a few times 10^9 cm^{-2}, a typical height between 1.5 and 2.5 nm, and appear to have relatively large base-to-height aspect ratios, consistent with a truncated pyramid morphology [12].

A schematic of the complete Schottky-diode structure is depicted in Fig. 1(b), while a scanning-electron-microscopy (SEM) image of a bonded device is shown in Fig. 1(c). The diodes are fabricated using standard GaAs processing technology and consist of 0.75-μm-deep mesas with 350–500 μm diameter, etched down to the n^+GaAs layer by reactive ion etching, onto which ring-shaped n-type (Ge/Au/Ni/Au) Ohmic contacts are evaporated and activated by rapid thermal annealing at 410 °C. On the top of the mesa, Ti/Pt/Au Schottky contacts are formed in a ring-shaped geometry with (175–250)-μm-wide rings at the edge of the mesas, whereas in the interior region of the rings, 80 nm of Ti is deposited in which nanoapertures with varying diameters between 350 nm and 5 μm are opened by electron-beam lithography for optical access. The μ-PL spectra are collected using a 40x objective with numerical aperture of 0.65 from a spot size smaller than 1.5 μm. The sample is cooled down to 100 K in a liquid N_2 (LN) flow cryostat. A variable-wavelength continuous-wave Ti:sapphire laser is used as the excitation source. In all biased experiments, the excitation power is sufficiently low (approximately 1 W/cm^2) to keep screening effects in the diode negligible. The signal is dispersed in a 0.75-m spectrograph with a 600 grooves/mm grating and is detected with a LN-cooled charge-coupled-device camera.

Specimens for HRTEM imaging are prepared in cross-sectional geometry by the standard sandwich technique, followed by mechanical grinding and low-voltage Ar^+ ion milling in the Gatan PIPS. HRTEM observations are carried out in a Jeol 2011 electron microscope operated at 200 kV. Local strain analysis is performed on numerous HRTEM images of QDs by GPA, where the reduced relative variation of the lattice fringe interplanar spacing is determined with respect to a reference region. Assuming the validity of Vegard's law, the GPA strain profile of a given QD can then be associated with compositional variations within the dot.

III. RESULTS AND DISCUSSION

The macro-PL spectrum obtained at 100 K from an unprocessed part of the sample is presented in Fig. 1(d) and exhibits characteristic broad emission from the QD layer in the 1.20–1.32 eV range, as well as intense heavy-hole (HH) and light-hole (LH) emission from the reference QW_1. The latter assignment is supported by the precise transition energy fitting discussed below. The sharp-peaked spectrum

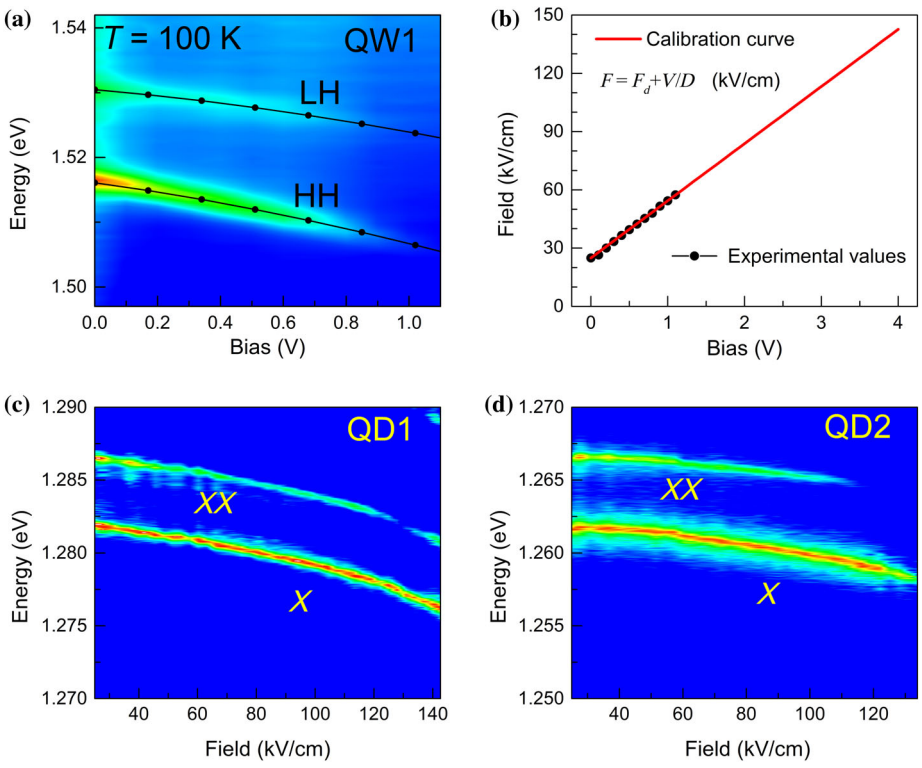

FIG. 2. (a) Variation of HH and LH transition energies of QW_1 as a function of external bias at 100 K. The dotted lines represent theoretical estimates of the QW_1 transitions. (b) Calibration curve (red line) between external bias and applied electric field extrapolated from the experimental points (dots) obtained by fitting the QW_1 transitions for each bias. (c),(d) PL images recorded for various values of the applied electric field at 100 K from two different single QDs.

underneath the QD macro-PL corresponds to micro-PL emission from a few QDs through a nanoaperture of relatively small size. In Fig. 2(a), the PL spectra of QW_1 are plotted as a function of external reverse bias in the range of 0 to 1.1 V, showing pronounced Stark shifts for both transitions reaching 10.8 meV for the HH peak as the bias increases to 1.1 V. Beyond this value, the QW_1 PL weakens drastically due to carrier escape and a decrease of oscillator strength caused by band bending. By comparison, the PL from single QDs persists up to 4 V of external bias, reflecting the much stronger carrier confinement in QDs. By solving the one-dimensional (1D) self-consistent Schrödinger-Poisson equation for QW_1 as a function of applied electric field with parameters taken from Ref. [28] and fitting the HH and LH transition energies for each bias shown as dotted lines in Fig. 2(a), we deduce the calibration curve of Fig. 2(b) between applied electric field F and external bias V. The obtained linear law indicated in the figure reproduces very well the one estimated for an *ideal* diode with an intrinsic region thickness of $D = 0.34$ μm, while its zero-bias limit F_d corresponds to an internal diode field of 25 kV/cm in good agreement with a Schottky-barrier height of 0.8 eV.

Using the calibration curve of Fig. 2(b), we present in Figs. 2(c) and 2(d) the PL images as a function of applied electric field for two different single PZ QDs, which are representative of measurements on more than a dozen QDs. In each case, the biexciton (XX) and neutral exciton (X) emission lines are identified according to their quadratic and linear power dependence, respectively, in conjunction with the absence of any other lines around the single QD emission. The linewidth of the X line is about 0.5–0.6 meV in both cases, very similar to the 100-K linewidths reported for (100) QDs under nonresonant excitation [29]. The excitation power level is kept constant for all values of external bias and is adjusted just below the saturation regime for the X state at zero bias. For clarity, the QD PL images in Fig. 2 are normalized to the X peak intensity. With increasing bias, the QD PL progressively drops in intensity, with the exposure times at high fields being 3 times larger compared to low fields. The main reason our experiments are limited to a reverse bias of 4 V is to keep leakage currents low. The continuous redshift of the QD lines throughout the applied bias range allows us to conclude that the external field applied to the structure "adds" to the internal PZ field of the QD, which is already a significant result in itself, as it demonstrates experimentally the importance of second-order PZ terms in strained zincblende nanostructures [26]. Because as illustrated in Fig. 1(a), if only linear PZ terms were applicable, then for the $(211)B$ orientation and the sign of bulk InAs e_{14} coefficient, the direction of the applied electric field would be antiparallel to the PZ field, thus, producing blueshifts instead of the observed redshifts. In Fig. 2(c), we observe for the X transition of QD_1 a redshift of about 5.8 meV for the first 140 kV/cm of applied electric field, which is already approximately 2.5 times larger than the respective Stark shifts observed in (100) counterparts [30] in the same field range. Moreover, we observe that the Stark shift varies significantly from one QD to another. For instance, QD_2 in Fig. 2(d) gives a Stark shift of only 3.4 meV in the same field range. This cannot be attributed merely to QD size variation, as in this picture, QD_2 emitting at lower energies than QD_1 should be of larger QD size and thereby exhibit larger Stark shift, which is obviously not the case. These dot-dependent Stark shifts strongly suggest that not only the dot size but also the In content varies from one dot to another. In order to explain the observed shifts, we resort to quantitative HRTEM methods to obtain direct information about the strain state and In-content profile of our QDs.

HRTEM imaging along the $[01\bar{1}]$ and $[\bar{1}11]$ projection directions shows that the QDs tend to adopt an anisotropic pyramidal shape elongated along the $[\bar{1}11]$ direction with a base-aspect ratio in the range of 1.2–1.4 [31]. In Fig. 3(a), a typical HRTEM image of a QD is depicted along the $[01\bar{1}]$ projection direction. Despite the presence of intense strain contrast, an approximate value of the QD width of 8–10 nm, a QD height of about 2–3 nm, and a wetting layer (WL) thickness smaller than 1 nm can be determined. No crystal defects are observed in the QD, implying the absence of plastic relaxation. For GPA strain measurements, a $g/3$ Gaussian mask corresponding to 1-nm spatial resolution in image space is placed around each of the two noncollinear 111-type spatial frequencies in the fast-Fourier-transform diffractogram of the HRTEM image. The underlying GaAs layer is used as a reference region. In the GPA strain map of Fig. 3(b), a zero average in-plane strain $\varepsilon_{xx} = 0$ is determined, suggesting full registration of the two lattices and elastically strained QDs. Small deviations of the ε_{xx} strain from the average value may arise due to thickness fluctuations of the sample in the area of interest and can be neglected. Conversely, a significant variation of the GPA strain along the growth direction is observed in Fig. 3(c). As depicted in the ε_{zz} line profile of Fig. 3(d) taken along the dotted arrow in Fig. 3(c), the out-of-plane strain gradually increases from $\varepsilon_{zz} = 0.042 \pm 0.001$ near the GaAs/InAs interface to almost 0.111 ± 0.001 at the apex region of the QD and then rapidly descends to zero at the QD apex/GaAs cap-layer interface. This trend is observed in all QDs studied, though with different ε_{zz} range of values. The corresponding ε_{zz} profile across the WL starts from about zero just above GaAs and reaches a maximum value of 0.042 ± 0.001, suggesting significant intermixing [32].

Subsequently, the elastic response of pure InAs QDs is estimated assuming that the dots are under biaxial strain and following the formulation of Hammerschmidt *et al.* [33]. The calculation of Poisson's ratio and the strain tensor along the [211] direction of the zincblende lattice, in conjunction with the bulk lattice parameters of GaAs

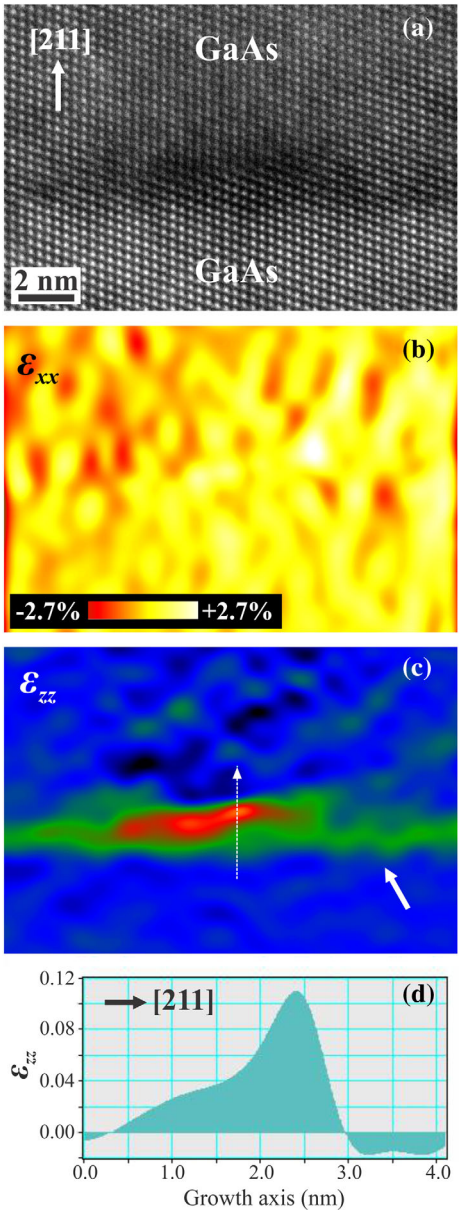

FIG. 3. (a) HRTEM image depicting an InAs QD embedded in GaAs(211)B along the [01$\bar{1}$] projection direction. (b) Corresponding GPA strain map showing an average $\varepsilon_{xx} = 0$ in-plane strain (color bar). (c) GPA strain map along the growth direction illustrating the variation of the ε_{zz} strain inside the QD with the GaAs lattice as reference. The shape of the QD is roughly delineated, while the tilted arrow denotes the WL. (d) Corresponding line profile of the ε_{zz} strain along the dotted arrow in (c) showing the progressive increase of ε_{zz} from the base towards the apex region of the QD.

and InAs, lead to the theoretical InAs-on-GaAs(211) $\varepsilon_{zz} = 0.1201$ GPA strain value. Hence, introducing the effective out-of-plane d-spacing values of the QDs extrapolated from our experimental GPA strain measurements into Vegard's law, we extract the chemical composition profiles of the QDs. For the QD of Fig. 3, the In content in the QD increases from $x_{\mathrm{QD}} = 35\%$ near the base to 92% ($\pm 1\%$) at the apex of the QD, suggesting that Ga segregates in the QD lattice mainly at the initial stages of QD growth. Similarly, the In content in the WL increases from zero at the interface to about $35\% \pm 1\%$, implying that it should be considered as an $\mathrm{In}_x\mathrm{Ga}_{1-x}\mathrm{As}$ alloy. Among the different QDs studied by GPA, the average In content at the base region is $\langle x_{\mathrm{QD}} \rangle = 25\% \pm 3\%$, while at the apex $\langle x_{\mathrm{QD}} \rangle = 70\% \pm 6\%$ with the maximum value of $x_{\mathrm{QD}} = 92\% \pm 1\%$ corresponding to the dot of Fig. 3.

Next, we try to simulate the observed transition energies and Stark shifts of our (211)B InAs QDs using a graded In-composition potential profile according to the conclusions of the preceding strain analysis. This is achieved by solving a 1D Schrödinger equation in the envelope function approximation using the NEXTNANO^3 semiconductor nanodevice simulator [34] including strain and PZ effects in the (211)B orientation. Material parameters are taken from Ref. [28]. The 1D simplification is justified in our case by the large aspect ratio of the QDs, implying that quantum confinement along the growth direction is much stronger compared to lateral confinement and the fact that the applied electric field is parallel to the growth axis leaving uncoupled the other quantization directions. An independent confirmation of the small lateral confinement energies in our system derives from the observation of s-p splittings of about 30 meV in photoluminescence excitation spectroscopy of single QDs. The QD height is fixed to 2 nm, keeping with AFM and HRTEM results. Then, we try several In profiles in order to reproduce the X-transition energy and the Stark shift of QD_1 in Fig. 2(c). For this particular QD, excellent fitting is obtained in Fig. 4(a), assuming a linear In profile starting from 30% at the base and reaching 74% at the apex of the dot. It should be noted here that the X-transition energy is quite sensitive to the average In content in the QD but not so much to the steepness of the In profile. As an example, for pure InAs QDs, the X-transition energy is estimated 0.26 eV lower than the 1.282 eV of QD_1. On the other hand, if instead of the 30% to 74% profile, we assume 0% to 100%, the X-transition energy merely changes by 6 meV. The steepness of the In profile, however, can have a notable effect on the Stark-shift curve. In the above estimates and fitting, the *nonlinear* PZ effect is been implicitly taken into account, using the second-order PZ coefficients of Bester *et al.* [26]. It is important to stress that without the nonlinear PZ effect, it is impossible to reproduce the observed redshifts. This is elucidated in Fig. 4(a), where we compare the best-fitting solid curve including the nonlinear PZ effect with the dash-dotted line produced assuming only a linear PZ coefficient and which clearly predicts a blueshifting behavior, unlike the experimental observation. This comparison constitutes a clear experimental verification of the importance of nonlinear PZ effects in heavily strained zincblende nanostructures.

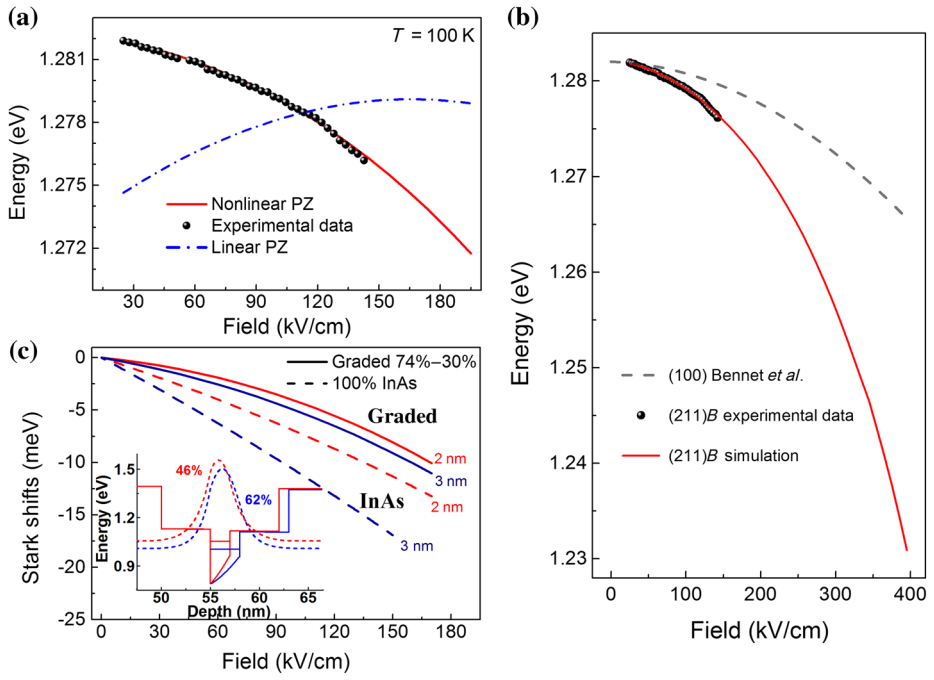

FIG. 4. (a) Experimental values (dots) of the QD X-transition energy versus applied electric field and calculated curve (red line) including nonlinear PZ terms. For comparison, the calculated curve with only linear PZ terms taken into account is also shown (dashed line). (b) Comparison of Stark shifts between $(211)B$ and (100) QDs showing the potential of PZ QDs in obtaining enormous Stark shifts compared to non-PZ QDs. (c) Calculated Stark shifts of the X-transition energy of QDs with heights of 2 and 3 nm, either for pure InAs (dashed lines) or for graded 74% to 30% In-content profile (solid lines). The inset depicts the conduction-band profiles and respective electron ground wave functions for the 2- and 3-nm-graded QDs at zero-applied electric field. The numbers in each case represent the probability of finding the electron inside the dot.

In Fig. 4(b), we extend the calculated Stark shifts for QD_1 up to 400 kV/cm in order to compare with the reported experimental data for non-PZ (100) InAs QDs [30]. A Stark shift greater than 50 meV is estimated for our $(211)B$ QDs at 400 kV/cm, about 3 times larger than the corresponding Stark shift of (100) QDs, demonstrating the large potential of these PZ dots towards the implementation of broadly tunable single0photon emitters at high temperatures. Finally, in Fig. 4(c), we plot the estimated Stark shifts in the case of pure $(211)B$ InAs QDs (dashed lines) or 30%–74% graded In profile $(211)B$ In(Ga)As QDs (solid lines) for two different QD heights of 2 and 3 nm. The curves follow the expected trend in the sense that the larger Stark shifts correspond to the pure and larger QDs, with the shifts almost doubling with respect to the graded QDs in the first 150 kV/cm. Taking a closer look, however, we realize that the 2- and 3-nm-graded In curves are unexpectedly close to each other, unlike the 2- and 3-nm curves for pure InAs QDs, which vary substantially. Following several simulation runs, this behavior is attributed to the fact that in the case of the relatively shallow 2-nm-graded InAs QDs, the carrier wave functions under the influence of the electric field "spread out" into the adjacent GaAs layers, a situation which increases their Stark tuning. This effect disappears as the QD levels become deeper. The different confinement in the two cases is illustrated in the inset of Fig. 4(c), where the probability to find the ground electron inside the 2-nm-graded QD is barely 46.4%, already at zero-applied electric field, whereas the same probability rises to 62.5% for the 3-nm-graded QD. In other words, enhancing further the tunability of these single-photon emitters should not only involve making the QDs larger and of pure In content but should also involve a careful design of the surrounding QW material.

The data of Fig. 4(a) can also be fitted using the equation $E = E_0 + pF + \beta F^2$ with $F > 0$, giving a dipole moment of $p = -4\ \mu\text{eV kV}^{-1}\,\text{cm}$ and a polarizability $\beta = -0.25\ \mu\text{eV kV}^{-2}\,\text{cm}^2$. These values can be compared with $p = -2.4\ \mu\text{eV kV}^{-1}\,\text{cm}$ and $\beta = -0.10\ \mu\text{eV kV}^{-2}\,\text{cm}^2$ in the work of Bennet *et al.* [30]. The higher negative value of the dipole moment in our case can be attributed to the nonlinear PZ field, which, in addition to the composition gradient, pushes further the holes towards the apex of the dots. On the other hand, the significantly larger polarizability in our case cannot be simply attributed to a larger QD height, as our dots emit at 1.28 versus 1.32 eV in Bennett *et al.* [30], energies which are not so different to justify such variation in dot size and polarizability. We suggest that the enhanced polarizability in our dots is at least in part related to the field-induced spreading of the dot wave functions into the adjacent GaAs layers, which as mentioned above, increases significantly their Stark tunings.

IV. CONCLUSION

In summary, we observe enhanced Stark tunings of single exciton lines of $(211)B$ InAs QDs at 100 K, due to the internal PZ field present in these nanostructures. The observed Stark shifts are at least a factor of 2.5 higher compared to standard non-PZ (100) InAs QDs, making this PZ QD system quite suitable for the implementation of tunable single-photon emitters at high temperatures. To account quantitatively for the observed transition energies and Stark shifts, we utilize a graded In-composition

potential profile, as deduced from GPA strain analysis on HRTEM images of the QDs. The direction of the observed redshifts clearly demonstrates that the PZ field is opposite of that predicted based on bulk InAs PZ coefficients. Our findings are in excellent agreement with recent theory taking into account nonlinear piezoelectric effects in highly strained InAs and have wide implications for the understanding of strained nanostructures grown along polar directions, such as, for instance, nanowire heterostructures grown along {111} crystallographic orientations.

ACKNOWLEDGMENTS

This work is co-financed by the European Union (European Social Fund—ESF) and Greek national funds through the Operational Program "Education and Lifelong Learning" of the National Strategic Reference Framework (NSRF)–Research Funding Program THALES, Grant No. MIS 377292, "NANOPHOS".

[1] M. Pelton, C. Santori, J. Vucković, B. Zhang, G. Solomon, J. Plant, and Y. Yamamoto, Efficient Source of Single Photons: A Single Quantum Dot in a Micropost Microcavity, Phys. Rev. Lett. **89**, 233602 (2002).

[2] N. Akopian, N. H. Lindner, E. Poem, Y. Berlatzky, J. Avron, D. Gershoni, B. D. Gerardot, and P. M. Petroff, Entangled Photon Pairs from Semiconductor Quantum Dots, Phys. Rev. Lett. **96**, 130501 (2006).

[3] C. Santori, D. Fattal, J. Vucković, G. S. Solomon, and Y. Yamamoto, Indistinguishable photons from a single-photon device, Nature (London) **419**, 594 (2002).

[4] S. Kako, C. Santori, K. Hoshino, S. Götzinger, Y. Yamamoto, and Y. Arakawa, A gallium nitride single-photon source operating at 200 K, Nat. Mater. **5**, 887 (2006).

[5] A. Schliwa, M. Winkelnkemper, A. Lochmann, E. Stock, and D. Bimberg, In(Ga)As/GaAs quantum dots grown on a (111) surface as ideal sources of entangled photon pairs, Phys. Rev. B **80**, 161307 (2009).

[6] R. Singh and G. Bester, Nanowire Quantum Dots as an Ideal Source of Entangled Photon Pairs, Phys. Rev. Lett. **103**, 063601 (2009).

[7] S. Germanis, A. Beveratos, G. E. Dialynas, G. Deligeorgis, P. G. Savvidis, Z. Hatzopoulos, and N. T. Pelekanos, Piezoelectric InAs/GaAs quantum dots with reduced fine-structure splitting for the generation of entangled photons, Phys. Rev. B **86**, 035323 (2012).

[8] M. Larqué, I. Robert-Philip, and A. Beveratos, Bell inequalities and density matrix for polarization-entangled photons out of a two-photon cascade in a single quantum dot, Phys. Rev. A **77**, 042118 (2008).

[9] A. K. Nowak, S. L. Portalupi, V. Giesz, O. Gazzano, C. Dal Savio, P.-F. Braun, K. Karrai, C. Arnold, L. Lanco, I. Sagnes, A. Lemaître, and P. Senellart, Deterministic and electrically tunable bright single-photon source, Nat. Commun. **5**, 3240 (2014).

[10] R. B. Patel, A. J. Bennett, I. Farrer, C. A. Nicoll, D. A. Ritchie, and A. J. Shields, Two-photon interference of the emission from electrically tunable remote quantum dots, Nat. Photonics**4**, 632 (2010).

[11] A. J. Bennett, M. A. Pooley, R. M. Stevenson, M. B. Ward, R. B. Patel, A. B. de la Giroday, N. Sköld, I. Farrer, C. A. Nicoll, D. A. Ritchie, and A. J. Shields, Electric-field-induced coherent coupling of the exciton states in a single quantum dot, Nat. Phys. **6**, 947 (2010).

[12] G. E. Dialynas, S. Kalliakos, C. Xenogianni, M. Androulidaki, T. Kehagias, P. Komninou, P. G. Savvidis, Z. Hatzopoulos, and N. T. Pelekanos, Piezoelectric InAs $(211)B$ quantum dots grown by molecular beam epitaxy: Structural and optical properties, J. Appl. Phys. **108**, 103525 (2010).

[13] G. E. Dialynas, A. Pantazis, Z. Hatzopoulos, M. Androulidaki, K. Tsagaraki, G. Konstantinidis, C. Xenogianni, E. Trichas, S. Tsintzos, P. G. Savvidis, and N. T. Pelekanos, InAs nanostructures on polar GaAs surfaces, Int. J. Nanotechnology **6**, 124 (2009).

[14] D. L. Smith and C. Mailhiot, Theory of semiconductor superlattice electronic structure, Rev. Mod. Phys. **62**, 173 (1990).

[15] R. M. Martin, Piezoelectricity, Phys. Rev. B **5**, 1607 (1972).

[16] W. A. Harrison, Effective charges, and piezoelectricity, Phys. Rev. B **10**, 767 (1974).

[17] G. Arlt and P. Quadflieg, Piezoelectricity in III–V compounds with a phenomenological analysis of the piezoelectric effect, Phys. Status Solidi **25**, 323 (1968).

[18] A. D. Corso, R. Resta, and S. Baroni, Nonlinear piezoelectricity in CdTe, Phys. Rev. B **47**, 16252 (1993).

[19] J. L. Sánchez-Rojas, A. Sacedón, F. González-Sanz, E. Calleja, and E. Muñoz, Dependence on the In concentration of the piezoelectric field in $(111)B$ InGaAs/GaAs strained heterostructures, Appl. Phys. Lett. **65**, 2042 (1994).

[20] R. André, C. Deshayes, J. Cibert, L. S. Dang, S. Tatarenko, and K. Saminadayar, Optical studies of the piezoelectric effect in (111)-oriented $CdTe/Cd_{1-x}Zn_xTe$ strained quantum wells, Phys. Rev. B **42**, 11392 (1990).

[21] R. André, C. Bodin, J. Cibert, L. S. Dang, and G. Feuillet, Non-linear piezoelectric effect in CdTe and CdZnTe, J. Phys. I (France) **03**, 429 (1993).

[22] S. Sanguinetti, M. Gurioli, E. Grilli, M. Guzzi, and M. Henini, Piezoelectric-induced quantum-confined Stark effect in self-assembled InAs quantum dots grown on (N11) GaAs substrates, Appl. Phys. Lett. **77**, 1982 (2000).

[23] M. Gurioli, S. Sanguinetti, and M. Henini, Dynamic quantum-confined Stark effect in self-assembled InAs quantum dots, Appl. Phys. Lett. **78**, 931 (2001).

[24] F. Widmann, J. Simon, N. T. Pelekanos, B. Daudin, G. Feuillet, J. L. Rouvière, and G. Fishman, Giant piezoelectric effect in GaN self-assembled quantum dots, Microelectron. J. **30**, 353 (1999).

[25] J. Simon, N. Pelekanos, C. Adelmann, E. Martinez-Guerrero, R. André, B. Daudin, L. S. Dang, and H. Mariette, Direct comparison of recombination dynamics in cubic and hexagonal GaN/AlN quantum dots, Phys. Rev. B **68**, 035312 (2003).

[26] G. Bester, X. Wu, D. Vanderbilt, and A. Zunger, Importance of Second-Order Piezoelectric Effects in Zinc-Blende Semiconductors, Phys. Rev. Lett. **96**, 187602 (2006).

[27] M. J. Hÿtch, E. Snoeck, and R. Kilaas, Quantitative measurement of displacement and strain fields from HREM micrographs, Ultramicroscopy **74**, 131 (1998).

[28] I. Vurgaftman, J. R. Meyer, and L. R. Ram-Mohan, Band parameters for III–V compound semiconductors and their alloys, J. Appl. Phys. **89**, 5815 (2001).

[29] C. Kammerer, C. Voisin, G. Cassabois, C. Delalande, P. Roussignol, F. Klopf, J. P. Reithmaier, A. Forchel, and J. M. Gérard, Line narrowing in single semiconductor quantum dots: Toward the control of environment effects, Phys. Rev. B **66**, 041306 (2002).

[30] A. J. Bennett, R. B. Patel, J. Skiba-Szymanska, C. A. Nicoll, I. Farrer, D. A. Ritchie, and A. J. Shields, Giant Stark effect in the emission of single semiconductor quantum dots, Appl. Phys. Lett. **97**, 031104 (2010).

[31] N. Florini, G. P. Dimitrakopulos, J. Kioseoglou, S. Germanis, C. Katsidis, Z. Hatzopoulos, N. T. Pelekanos, and T. Kehagias, Structure, strain, and composition profiling of InAs/GaAs (211)B quantum dot superlattices, J. Appl. Phys. **119**, 034304 (2016).

[32] C. Heyn, A. Bolz, T. Maltezopoulos, R. L. Johnson, and W. Hansen, Intermixing in self-assembled InAs quantum dot formation, J. Cryst. Growth **278**, 46 (2005).

[33] T. Hammerschmidt, P. Kratzer, and M. Scheffler, Elastic response of cubic crystals to biaxial strain: Analytic results and comparison to density functional theory for InAs, Phys. Rev. B **75**, 235328 (2007).

[34] S. Birner, T. Zibold, T. Andlauer, T. Kubis, M. Sabathil, A. Trellakis, and P. Vogl, Nextnano: General purpose 3-D simulations, IEEE Trans. Electron Devices **54**, 2137 (2007).